Coherent beam combination of seven 1.5 μm fiber amplifiers through up to 1 km atmospheric turbulence: Near and Far Fields experimental analysis

Bastien Rouzé, Laurent Lombard, Hermance Jacqmin, Anasthase Liméry, Anne Durécu, Pierre Bourdon

Coherent beam combination of seven 1.5 µm fiber amplifiers through up to 1 km atmospheric turbulence: Near and Far Fields experimental analysis

BASTIEN ROUZE,[1] LAURENT LOMBARD,[1,*] HERMANCE JACQMIN,[1] ANASTHASE LIMERY,[1] ANNE DURECU,[1] AND PIERRE BOURDON[1]

[1]*DOTA, ONERA, Université Paris Saclay –91120 Palaiseau, France*
**laurent.lombard@onera.fr*

Abstract: A laser testbed based on active coherent beam combination (CBC) of seven 1.5 µm, 3 W fiber amplifiers was developed for applications requiring high power such as power density deposition on target or free space laser communication. For the first time to our knowledge, the frequency-tagging LOCSET technique (Locking of Optical Coherence by Single-detector Electronic-frequency Tagging) was implemented in the field in real atmospheric turbulence conditions in a target-in-the-loop configuration. Successful combination was achieved after horizontal propagation of 311 m and 1 km, at 1.5 m above the ground, while the estimated average turbulence strength was $C_n^2 \sim 4.10^{-14}$ m$^{-2/3}$. In this paper, we present the CBC laser bench and an embedded near-field interferometer called PISTIL (PISton and TILt) able to measure the relative phase shift of each emitter. We show that this measurement can provide information on relative turbulence-induced phase variation of the combined laser beams. In particular, the far-field beam envelope wandering can be estimated through this diagnosis. Results are supported by an analytical model and confirmed by numerical post-analysis of measured far-field interference. This additional interferometer may improve CBC beam pointing through turbulence.

1. Introduction

Today, increasing laser power is a key challenge for many areas of physics and defense [1-3]. This laser power increase brings out new limits such as optical damage or nonlinear effects in power amplifiers [4-6]. To overcome these limits, the coherent beam combination (CBC) of elementary laser sources is an interesting solution, enabling modularity, robustness and efficiency [7-10].

Typical CBC architectures are made of several power amplifiers seeded by a single CW master oscillator. In a tiled CBC configuration, the amplified laser beams are spatially arranged in the pupil plane, i.e. the near field (NF), then propagate in free space and eventually interfere on a target in the far field (FF). Constructive interference occurs when the phase differences between all channels are minimized on the target. This can be achieved using a feedback loop to compensate for the phase delay (piston) using phase modulators integrated in each channel. The combination quality is quantified by the residual phase error between all channels in closed loop or the relative power contained in the central lobe of the interference pattern [10, 11].

The target itself can be included in the feedback loop, in a scheme referred as 'target-in-the-loop' (TIL) [12]. TIL-CBC faces different challenges. First it should take into account the phase variations experienced by the beams from the master laser to the target because of fiber amplifiers phase noise but also atmospheric turbulences in case of outdoor experiments. Secondly, it has to perform phasing from the backscattered signal knowing that useful signal lie only in the central lobe backscattering. The problematic of TIL-CBC has been extensively studied in simulations with different situations, including weak to moderate turbulences and

various laser designs (e.g., the number of emitters, phase correction strategies, etc.) [13-20]. Most of those simulations agree on a Power in the Bucket of about 33% for km range propagation through atmospheric turbulence and that piston-only turbulence compensation is sufficient for weak to moderate turbulences; yet can be limited by power-leakage from the central lobe to the side lobes on the target. To our knowledge, the piston-only turbulence compensation strategy, which alleviate the TIL-CBC system complexity, has been tested in the laboratory under artificial turbulence conditions or at short distances [21-24]. Turbulence compensation with a cooperative target has been demonstrated up to 7 km using TIL-CBC devices based on individual controls of every sub-pupils piston, tip and tilt [25, 26]. Most experimental TIL-CBC demonstrations are based on SPGD (Stochastic Parallel Gradient Descent) [21, 22, 25-27] and LOCSET (Locking of Optical Coherence by Single-detector Electronic-frequency Tagging) [23, 28] phase-locking algorithms. On one hand, LOCSET CBC lasers are used until now only for laboratory demonstrations. On the other hand, improved SPGD algorithms can enable TIL-CBC on an extended target using a speckle-based metric [29], or automatic tip-tilt fiber control for strong turbulence mitigation [30, 31].

In this paper, we present successful outdoor TIL-CBC using piston-only turbulence compensation and the LOCSET algorithm with a 7-fiber-amplifiers system emitter arranged in a tiled hexagonal mesh. Target distance ranges from 300 m to 1 km, and the beam propagates at 1.5 m height with various turbulence conditions (turbulence strength C_n^2 up to 10^{-13} $m^{-2/3}$). Stable constructive interference has been obtained on the target in the FF using phase delays (pistons) compensation. However, uncorrected residual perturbations from turbulence generate power-leakage as mentioned before. A local NF segmented wavefront analyzer called PISTIL (PIston and TILt) [32-35] was installed to measure the relative phase piston of each emitter. A CBC beam envelope wandering model is proposed to explain power-leakage, which is experimentally characterized by both the FF interference pattern behavior and NF PISTIL analysis.

2. LASBE TIL-CBC testbed description

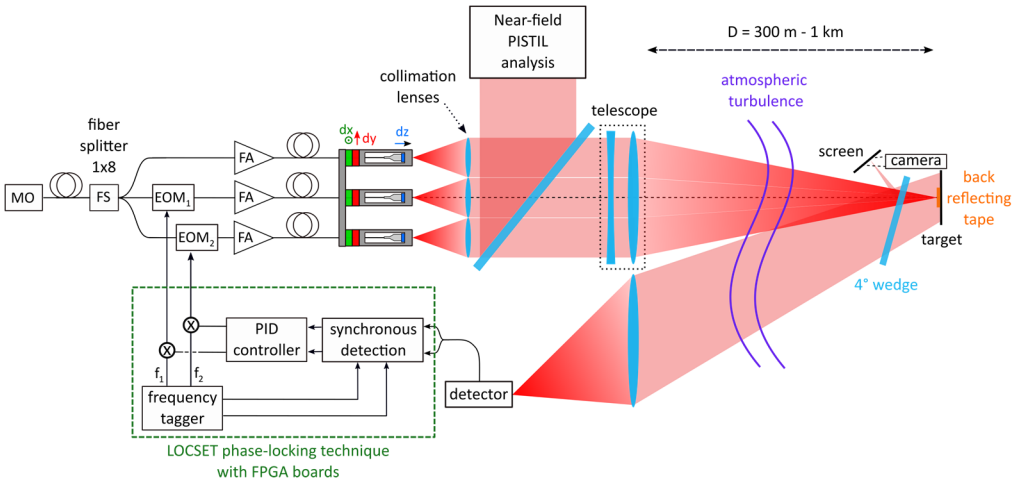

Fig. 1: Layout of the TIL-CBC with the LASBE testbed. Laser sources propagate through atmospheric turbulence a distance D to a target where a reflecting tape lies. Backscattered light is collected by the reception unit. In order to observe the combination pattern, the target plane is duplicated onto a camera by the use of a 4° wedged window. MO: Master Oscillator. FS: Fiber splitter. EOM: Electro-optical modulator. FA: Fiber amplifier.

The LASBE project purpose is to maximize the coherently combined power of seven laser beams on a remote target through atmospheric turbulence with active phase control based on the LOCSET technique [23].

2.1 Fiber amplifiers and optical head

The testbed includes a 7-channel MOPA (Master Oscillator Power Amplifier) laser system as illustrated on Fig. 1. Every element of the laser system contains polarization maintaining fibers. The seeder is a narrow linewidth distributed feedback (DFB) laser source (Gooch & Housego) delivering 40 mW at 1545 nm. This wavelength combines low atmospheric absorption and high gain in erbium/ytterbium doped fiber amplifiers. The MO output is split into 7 channels using a standard 1 to 8 fiber splitter (one is not used). Six fiber-coupled electro-optic modulators (EOM) ensure frequency tagging and laser beam phase control of 6 channels using the LOCSET technique. Each channel is tagged with low-depth modulation at a specific frequency. The wavefront is backscattered to the reception unit made of a large lens and a photodetector. Then each frequency is demodulated to recover the corresponding 6 phase error signals to be minimized by the controller. The phase of the central laser beam is used as a reference so that the phase locking loop drives the phase difference between each channel and the reference to zero.

Each channel path accumulates, the phase noise from propagation (atmospheric turbulence) and from the fibered path (amplifier phase noise). According to [36], the typical optical turbulence coherence time is on the order of 1 to 10 ms (cutoff frequency ranging from 100 Hz to 1 kHz). On the other hand, the accumulated phase noise of fiber amplifiers is up to $f_{noise} = 10$ kHz [9].

In order to properly sample the phase noise and distinguish the contribution of different channels, the tagging frequencies must fit within an octave and should be spaced by at least $\sim 10 \times f_{noise}$. This leads to tagging frequencies ranging from $F_1 = 10 \times N \times f_{noise} = 0.6$ MHz to $F_6 = 10 \times (2N - 2) \times f_{noise} = 1$ MHz with $N = 6$ and $f_{noise} = 10$ kHz [9]. The effective bandwidth of the control loop is 30 kHz. Moreover, the EOM (Ixblue) has a 150 MHz bandwidth and fulfills this requirement.

The EOM outputs seed 7 commercial erbium/ytterbium-doped fiber amplifiers (Lumibird) delivering 3 W each and integrated in a rack. Special care was taken to limit the vibrations induced by fans, identified in previous work as the main phase noise contribution [37].

The fiber amplifier outputs are maintained in individual mounts with three adjustments: transverse translations (x,y) ensured by two superimposed piezomotors (Physik Instrumente) and longitudinal translation in the beam propagation direction (z) ensured by a manual screw. The optical head, including the output fibers mounts, has been designed in our laboratory at ONERA (Office National d'Etudes et de Recherches Aérospatiales). Fiber outputs were collimated by 100 mm focal length, 1 inch diameter lenses arranged in a compact hexagonal array. The distance between the centers of two adjacent lenses is 27 mm, leading to a pupil size of 80 mm (Fig. 2). Such a compact array is set to maximize the aperture (area) fill factor which is about 70% (ratio between the sub aperture surfaces to the global pupil surface) [17]. The sub-aperture fill factor (ratio between beam waist and lens radius) [10] is equal to 80% of the collimation lens radius. It has been optimized in order to maximize the on-target absolute PIB, resulting in a beam waist diameter of 20 mm. This configuration is a compromise between the lenses transmission and the relative PIB on target. In case of perfect co-phasing, the theoretical CBC interference figure (Fig. 2) in the far field will have the following central lobe diameter:

$$d_{CBC}^{th} = \frac{2.44\lambda D}{A}, \tag{1}$$

where D is the propagation distance (311 m or 1024 m), and A the aperture (pupil) diameter (multiplied by the telescope magnification).

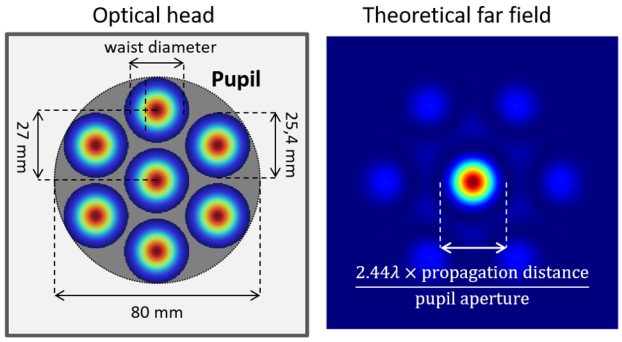

Fig. 2: (Left) Layout of the LASBE tiled pupil in the optical head. (Right) Theoretical co-phased CBC interference figure in the far field.

The lenses are fixed and the collimation of each beam can be adjusted by tuning the z axis position of the amplifier output fiber connectors. Far-field beam overlap is achieved by tuning the transverse positions (x,y) of each emitter with respect to the collimation lenses using the piezomotors.

2.2 Emission path

The seven collimated beams are focused on the target plane using a large diameter telescope made up of one divergent doublet and one convergent doublet with focal lengths of -420 mm and 500 mm, respectively. These optics and their mechanical mounts were designed at ONERA to minimize the optical aberrations and mechanical stress. The distance between the doublets is adjusted with a manual translation stage. The focusing distance ranges from 50 m to the km range. In the experiments, the propagation distance through atmospheric turbulence is ~70 m, ~300 m, or ~1 km and the beams are 1.5 m above the ground.

2.3 Target, reception path and error signal feedback

The target is made of a black surface (low albedo at 1.5 µm) and a reflecting tape with high albedo (~ 100× albedo ratio). The size of the tape will be chosen to be smaller than the central lobe of the CBC interference pattern, given by Eq.(1) (numerical data will be given in section 3). As shown in Fig. 1, emission and reception paths are distinct. Backscattered light is collected by a lens and focused on a photodetector (Thorlabs). The phase modulation translates into intensity modulation thanks to the central lobe selection made by the reflecting tape. The electrical signal is amplified and split into 6 channels. For each channel except the reference beam, a synchronous detection module including filtering stages generates an error signal proportional to the sine of the phase-shift between the considered channel and the reference channel [23, 28]. PI (proportional integrator) controllers drive to zero these error signals. Finally, each PI output is added to the tagging signal and fed into the corresponding EOM. Each step of the feedback loop (synchronous detection, PI controller, phase correction) is performed numerically using a FPGA device. To avoid the obsolescence of the phase-controller inputs, the propagation delay of the backscattered light should be lower than half of the coherence time of the optical turbulence (half a ms). In the case of a propagation up to 1 km in the air, such condition is valid (time delay in the range of µs).

2.4 PISTIL near-field interferometer

In between the collimation lenses and the emission telescope (Fig. 1), a 99/1 beamsplitter samples the beams toward a NF piston and tilt (PISTIL) interferometer. This interferometer includes a mask with holes arranged to sample the center of each emitted beam and a tri-directional hexagonal diffraction grating [32] which creates six equally tilted replicas for each sub beam. The six replicas of one sub beam interfere with the replicas of the six adjacent sub

beams, resulting in 12 patterns of 2-wave interferences (in case of 7 sub beams) in the interception plane, which is then imaged on a camera (Fig. 3, top left).

The interference figure is called hereafter a pistilogram. Exploitation of the pistilogram enables piston phase retrieval for each element in the NF [33-35]. So the phase retrieval via PISTIL leads to estimation of the 6 phase differences relative to the central fiber. Phases are unwrapped continuously with measurement time.

The technique has been tested in the laboratory (CBC distance of 15 m) with no or weak turbulence. It provided an estimate of the residual phase error (closed-loop rms value) of the LOCSET setup, which was $\lambda/70$ rms (average of 6 channels residual phase error rms). During closed-loop sequences, the interferometer successfully tracked perturbations induced by a slow motion applied to the optical bench, as illustrated on the bottom graph of Fig. 3. The NF wavefront composed of the 7 sub-pupil wavefronts can be represented for each frame as shown in Fig. 3.

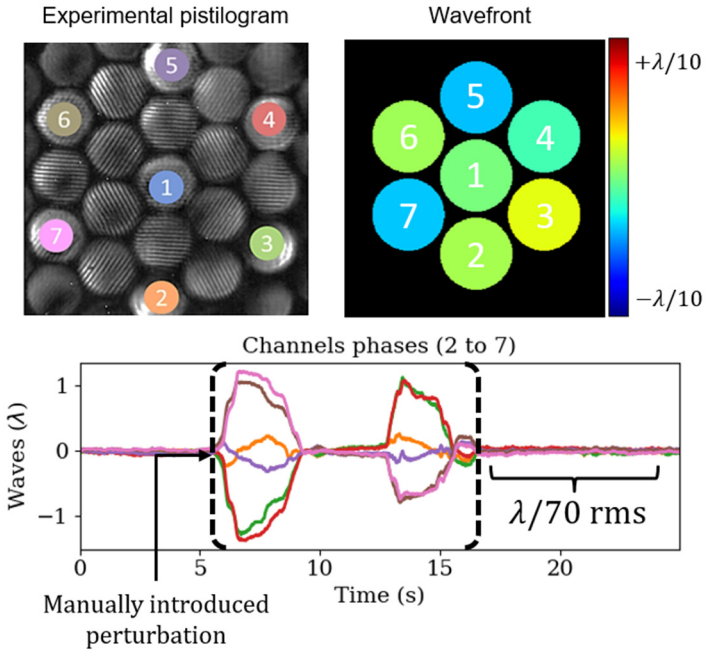

Fig. 3: (Top left) Experimental pistilogram (color circles indicate sub beams). (Top right) Reconstructed wavefront of one frame displaying the piston correction in waves for each of the 6 beams (central beam phase set to zero). (Bottom) Relative phase estimates by PISTIL during a closed-loop run (colors match with pistilogram). Perturbation is introduced to highlight the phase tracking of the laser near field.

In practice, an afocal system is used to adapt the NF beam size to the PISTIL system dimensions. The mask is defined by a hole pitch of 1.35 mm and a hole diameter of 0.6 mm. The grating has a period of 97 µm. An additional afocal system matches the pistilogram to the camera dimensions (XENICS InGaAs camera, 340x256 pixels, 30 µm pixel pitch, and 60 Hz frame rate). The effective PISTIL bandwidth is therefore less than 30 Hz and will not record the turbulence effects on the feedback loop faster than 30 Hz. The low-depth, high-frequency phase modulation used by LOCSET are unseen; the PISTIL fringes do not fade.

3. TIL-CBC measurements at 300 m and 1 km: conditions, operation and observations

3.1 Conditions for on-site measurements

The LASBE emitter/receiver system is mounted in a 3 stage vertical structure (Fig. 4, left). The lower stage contains the optical head with the 7 amplifier outputs emitting collimated beams upward. The middle stage contains the emission and reception paths. The upper stage is dedicated to the PISTIL interferometer. The system has been mounted and tested in the ONERA-Palaiseau facilities and then transported during the summer of July 2019 to the ONERA-Fauga facilities (South of France) where a 1-km long test field is available for outdoor free space experiments (Fig. 4, right). The LASBE system was installed into a dedicated laboratory (Fig. 4), whereas the target (with the reflecting tape, see Section 2.3) along with an optical characterization bench were installed in a mobile truck. The LASBE system output/input lenses are located 1.5 m above the ground. The setup is arranged as shown in Fig. 1. The target optical bench includes a 4° wedged reflecting window enabling non-invasive observation of the CBC FF using a magnified camera (RAPTOR OW1.7-VS-CL-640, 640x512 pixels, 15 µm pixel pitch, 30 Hz frame rate).

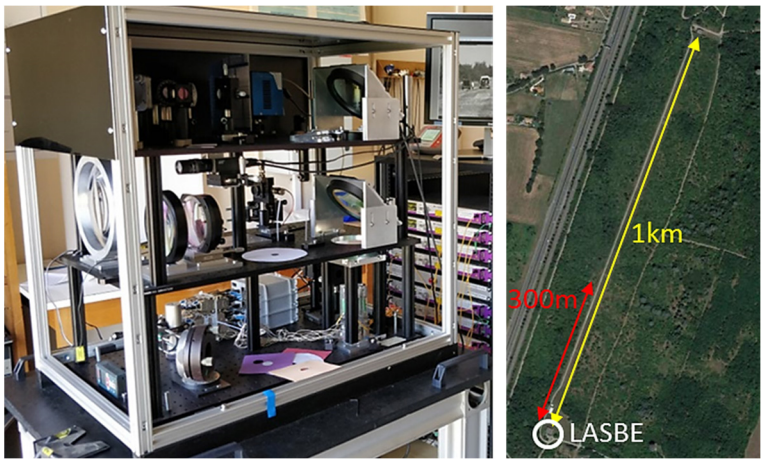

Fig. 4: (left) LASBE setup installed in the lab; (right) ONERA-Fauga 1 km free space test field overview. The testbed is installed in the lab (white circle), while the target is in a mobile truck to move it from 300 m (red arrow) up to 1 km (yellow arrow).

Weather conditions during LOCSET TIL-CBC experiments were measured using a local weather center located on the laser path 100 m away from the emitter. The average max/min local temperatures were 29°C/17°C, with constant 1 atm air pressure, and a low wind velocity (< 3 m/s) during the experiments. The turbulence strength C_n^2 and the Fried parameter r_0 were also continuously recorded using a BLS900 scintillometer (Scintec, 880 nm wavelength). Fig. 5 shows records of a typical day with strong variations from 10^{-14} $\mathrm{m}^{-2/3}$ up to 10^{-12} $\mathrm{m}^{-2/3}$. Most measurements were carried out from 14:00 to 01:00 under various turbulence conditions.

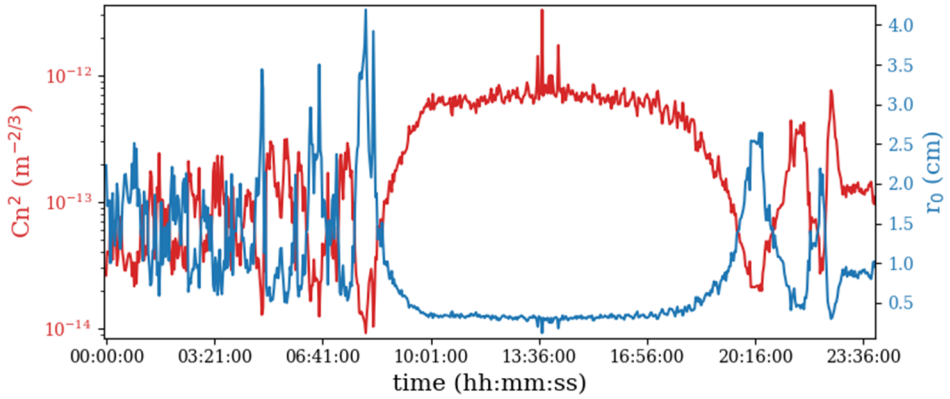

Fig. 5: Example of turbulence conditions at ONERA-Fauga test site, July 2019.

3.2 Operation of the LASBE TIL-CBC/LOCSET system and observations

The LASBE emitter is first coarsely directed towards the target by manually setting the global tip-tilt of the complete LASBE testbed using two translation stages, a camera, and a green laser attached to the bench. Then, fine global tip/tilt is adjusted using the central channel by maximizing the backscattered signal on the photodetector. Fine individual tip/tilt adjustment is repeated for each channel until each hits the target. Once the alignment is done, the LOCSET TIL-CBC feedback loop is closed. The LASBE coherent beam combination successfully worked under various C_n^2 conditions and distances (70 m, 311 m and 1024 m), with fringe contrasts of the FF interference pattern exceeding 80%.

Examples of the averaged CBC patterns are shown in Fig. 6 for both 311 m and 1024 m. The first column from the left shows the averaged FF images in the case of open loop sequences when D = 311 m (a) and D = 1024 m (e). As expected, (a) and (e) show no interference pattern as the fringes move faster than the acquisition time. The second column shows the corresponding averaged images of the FF pattern when the feedback loop is closed. The average pattern in (b), when D = 311 m, shows, as expected, an intense central lobe and 6 lower and equally intense lobes. The averaged pattern in (f), when D = 1024 m, shows a less expected triangular pattern with three main intense lobes. As will be discussed later, this is due to a global tip/tilt of the beam induced by turbulence.

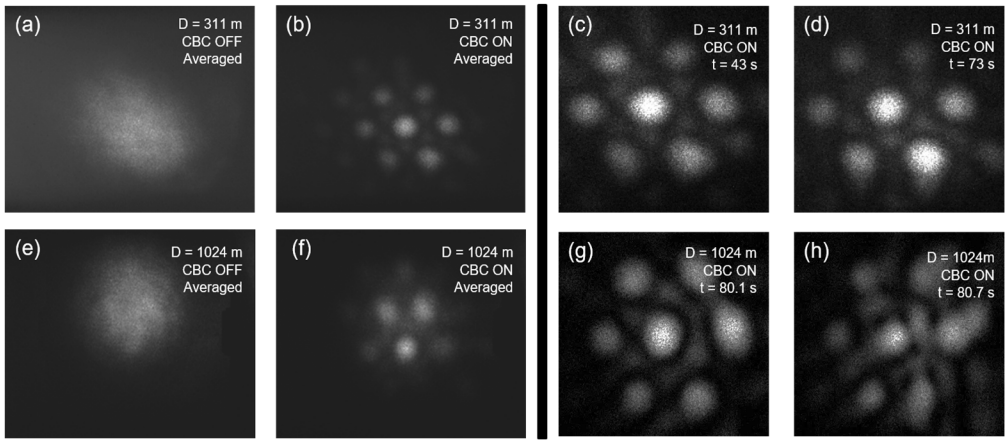

Fig. 6: FF images. (a) and (e): averaged FF images with feedback loop open (averaged speckle) for D = 311 m and D = 1024 m. (b) and (f): averaged FF images with feedback loop closed (CBC pattern) for the same distances. Images (c), (d) and (g), (h) show instantaneous frames

from the closed loop sequences to highlight power-leakage up to complete distortion of the pattern. Timestamps show the timescale of the disturbances.

Reviewing the recorded sequences, different perturbations can be observed at both 311 m and 1 km. In order to illustrate the beam wander effect (tip-tilt) of the interference pattern, we chose two instantaneous images from the recorded sequence of (b) shown in (c) and (d). A lateral shift of the irradiance distribution between (c) and (d) can be clearly observed at 311 m. Similarly, a lateral shift as well as a heavier distortion of the pattern appears between (g) and (h), selected from the sequence in (f) at 1 km. These experimental observations are thoroughly examined in the Section 4 of this paper. Note that such FF behaviors have been observed to a lesser extent in the reference simulations [14-18] (where weaker turbulence was used). In the following, we present the NF and FF experimental criteria that have been used to quantify the coherent beam combining performances.

First, the quality of the piston phase-locking on target is quantified by tracking the central lobe position variation in the focal plane. It presents a limited deviation up to 2 pixels rms (~ µrad scale tip/tilt) for all sequences, which confirms good performance for LOCSET TIL-CBC system.

Using Eq.(1), the central lobe dimension was estimated to be $d_{CBC}^{exp} = 14.6$ mm at 311 m and 41.2 mm at 1024 m (average values), consistent with the theoretical values: $d_{CBC}^{th} = 12.3$ mm and 40.4 mm, respectively. It is always near 2 times larger than the target (tape) reflective size (6 mm and 25 mm for the two distances).

To provide information about both the phase-locking performance and the observed irradiance shift, we first define a PIB-like metric, I_{PIB}, computed by integrating the camera intensity inside an area of diameter d_{CBC}^{exp} centered on the main lobe. We can compute an average combining efficiency or relative PIB, defined by I_{PIB}/I_{tot} where I_{tot} is the camera intensity integrated over a disc covering the side-lobes. The average combining efficiency is about 33% at 70 m, 23% at 311 m and 19% at 1 km. These experimental values are lower (by ~10%) than the theoretical simulations of CBC through turbulence from references [11, 14-16] (for the 7 beams case and a C_n^2 value an order of magnitude lower than the measured values in our experiments). This also indicates that further improvement is still possible.

Fig. 7 (top) shows I_{PIB} normalized by its max value in the case of a closed-open-closed feedback loop sequence during experiment at a distance $D = 311$ m (Fig. 6 (a) and (b)). The turbulence strength is of $C_n^2 = 2 \times 10^{-14}$ m$^{-2/3}$. When the feedback loop is closed, the amount of power deposited on the target is almost doubled (0.1 to 0.2 counts in average) compared to when the feedback loop is open (clearly discernable from t ~ 100 s to ~ 145 s).

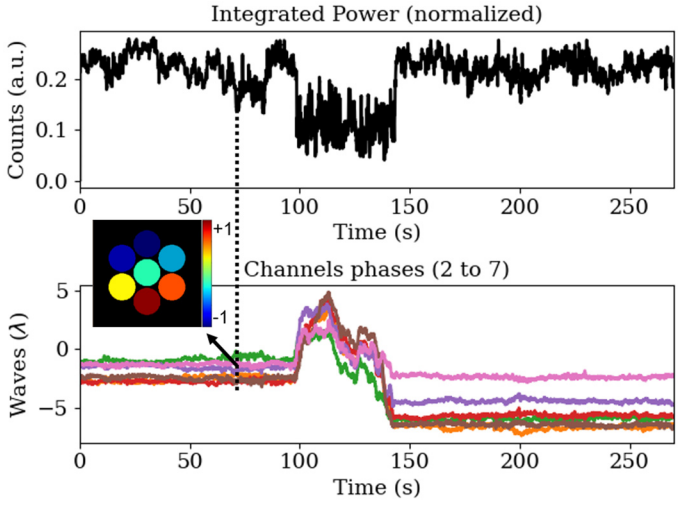

Fig. 7: CBC distance $D = 311$ m, turbulence strength $C_n^2 = 2.10^{-14}$ m$^{-2/3}$, feedback loop sequence : closed-open-closed. (top) FF main lobe relative power integrated into a d_{CBC}^{exp} area, from images recorded by the RAPTOR camera; (bottom) PISTIL phase (piston) tracking of the six ring beams. Inset: spatial display of the NF wavefront of the 6 beams plus the central channel.

At the same time, the PISTIL interferometer was measuring the relative phases at the optical head output (NF) of the LASBE emitter (Fig. 7, bottom). When the feedback loop is closed, PISTIL records the relative phase pistons applied by the feedback loop to the 6 beams to compensate for the turbulence variation. The measurement starts at the time of co-phasing, and thus very little deviation is observed until the feedback loop is open. It indicates that the phase shifts induced by turbulence are relatively mild.

When the feedback loop is open, PISTIL tracks the phase error due to the fiber amplifiers, which is more than 5λ per channel for the 50 s duration. Once the loop is closed again, phases are stabilized to new values that result in constructive interference in the FF.

Finally, the inset of Fig. 7 shows the typical wavefront made by the 6 beams plus the central channel set to zero when a decrease in the integrated I_{PIB} is observed in the closed-loop sequence. It is interesting to see that at times of power-leakage to the side lobes of the CBC pattern, the wavefronts take the form of a tip-tilt over the pupil, sampled by the piston corrections.

In the next section, we introduce the theoretical background explaining how the uncompensated turbulence results, to a first approximation, in a power leakage from the central lobe of the FF pattern to the side lobes.

4. Analysis of the CBC beam envelope in case of turbulence variation corrected by phase pistons

4.1 Interpretation

Performing beam combination using piston correction alone is limited to short range or weak to moderate turbulence strength ($\sim 10^{-14}$ m$^{-2/3}$). Whenever these conditions are not met, the first additional effect that can be observed is power-leakage from the central lobe of the CBC pattern, as pointed out in section 3. Power leakage is caused by residual turbulence-induced phase variations that cannot be corrected by piston alone. Stronger turbulence conditions ultimately end up in more distortions of the pattern.

In our experiments, the effect of atmospheric turbulence can be approximated either by a single, pupil-sized, dynamic tip-tilt or by a set of dynamic tip-tilts, depending on how the Fried parameter r_0 compares to the pupil diameter or sub-beams diameter. Indeed, variances calculations by Noll [38] state that a turbulence area of diameter r_0 is mainly represented by

tip-tilt Zernike polynomials. To estimate our Fried parameter range, we rescale the r_0 computed by the BLS900 (see Fig. 5, recorded at 880 nm) to the LASBE wavelength (1545 nm) for the C_n^2 values of our experiments ($\sim 1 \times 10^{-14}\,\mathrm{m}^{-2/3}$) using the $r_0 \propto D^{-3/5}\lambda^{6/5}$ relation. Additionally, as the beams are converging to the target, a last rescaling has to be applied to r_0 because of spherical wave propagation. This nearly doubles its value [39, 40], so that the upper bound of r_0 is now 10 cm at 311 m and 5 cm at 1024 m. Those values have to be compared to the pupil dimension (8 cm). Using this result, we can estimate that during our experiments, the atmospheric turbulence experienced by the laser beams was similar to a global tip/tilt (pupil size) at the 311 m distance and a few tip/tilts for the 1 km distance (in between the pupil and sub pupil sizes).

According to this very basic model, the main effects of turbulence on the global aperture wavefront are tip and tilt. Assuming this global tip-tilt will be compensated for a piston value relative to each sub aperture size (i.e., local mean of the tip-tilt), the residual turbulence effect will thus be a zero-mean tip-tilt on each beam path. Fig. 8 illustrates the logic with a tip angle α: the residual turbulence effect is obtained by subtracting the piston correction from the turbulence induced phase variation. The beams are then affected by the same tip-tilt residual phase. This should generate the observed leak, and correlate with the PISTIL measurements. This first order qualitative description of the FF behavior will be explained in more detail with the help of a simple analytical model in the next subsection.

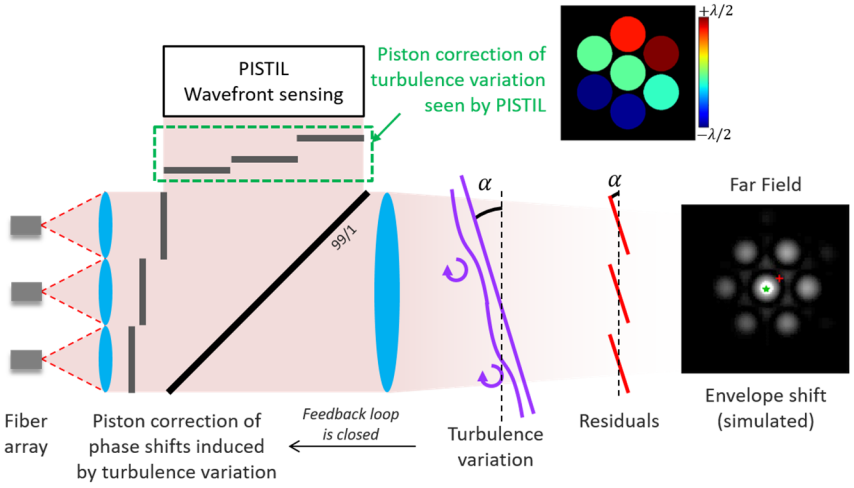

Fig. 8: Piston correction under atmospheric turbulence dominated by tip-tilt of angle α. The uncorrected residual phase on each channel results in a non-optimal irradiance distribution of the FF pattern, as illustrated by the simulated CBC pattern on the right. The red cross corresponds to the irradiance barycenter, and the green cross is the target.

4.2 Analytical model

To better understand the variation observed in the FF interference pattern with the residual tip-tilt variation per sub-beam in experimental piston correction, we propose a didactic 1D model of the CBC. Only the residual tip-tilt is considered (red slopes in Fig. 8). The model can easily be extended to the 2D case.

First, we consider 3 collimated Gaussian beams regularly arranged according to a hexagonal array inside the tiled laser pupil of diameter $3a$. The global aperture is truncated by the door function $\prod(x/3a)$. The reference Gaussian beam is noted $G(x)$ and has a similar sub aperture fill-factor than our laser (see section 2.1). So, each beam is truncated by its collimation lens of diameter $d \leq a$, via the door function $\prod(x/d)$. The NF amplitude (A_{NF}) of the laser can be expressed as follows:

$$A_{\mathrm{NF}}(x') \propto \left\{\left[G(x)\cdot\prod\left(\frac{x}{d}\right)\right] * \mathrm{Comb}_{\mathrm{a}}(x)\right\}(x')\cdot\Pi\left(\frac{x'}{3a}\right), \tag{2}$$

where $*$ stands for convolution, $\cdot$ for common product and $\mathrm{Comb}_{\mathrm{a}}(x)$ is a 1D Dirac Comb of period a. In order to ease the equations reading, the truncated Gaussian function is noted $G_{\mathrm{T}}(x) = G(x).\prod(x/d)$. The CBC, or FF amplitude (A_{FF}) is equal to the Fourier transform of Eq. (2), leading to

$$A_{\mathrm{FF}}(f_x) \propto \left\{\left[\widetilde{G_{\mathrm{T}}}(v_x)\cdot\mathrm{Comb}_{1/\mathrm{a}}(v_x)\right] * \mathrm{sinc}(3av_x)\right\}(f_x), \tag{3}$$

where $\widetilde{G_{\mathrm{T}}}$ is the Fourier transform of G_{T}. The convolution can be written as an integral, and Eq. (3) can be reduced to

$$A_{\mathrm{FF}}(f_x) \propto \sum_{k\in\mathbb{Z}} \widetilde{G_{\mathrm{T}}}\left(\frac{k}{a}\right)\mathrm{sinc}\left[3a\left(f_x-\frac{k}{a}\right)\right]. \tag{4}$$

The interference pattern amplitude is now described. The envelope is given by the Fourier transform of the truncated Gaussian function. If a residual phase tilt α is now taken into account for each sub beam of the laser as illustrated by Fig. 10, so that Eq. (2) and FF amplitude in Eq.(4) become:

$$A_{\mathrm{NF}}(x') \propto \{[G_T(x)\exp(i2\pi\alpha x)] * \mathrm{Comb}_{\mathrm{a}}(x)\}(x')\cdot\Pi\left(\frac{x'}{3a}\right), \tag{5}$$

$$A_{\mathrm{FF}}(f_x) \propto \sum_{k\in\mathbb{Z}} \widetilde{G_{\mathrm{T}}}\left(\frac{k}{a}-\alpha\right)\mathrm{sinc}\left[3a\left(f_x-\frac{k}{a}\right)\right] = \sum_{k\in\mathbb{Z}} U_k(f_x). \tag{6}$$

The difference between Eq.(4) and Eq.(6) is the weighting of the sinc functions, which is now a function of the residual tilt α distributed on each sub-beam. Then, if the tilt α varies, so does the $\widetilde{G_{\mathrm{T}}}$ function for each amplitude lobe, which affects the FF the CBC pattern's irradiance (as shown in Fig. 6 and Fig. 9):

$$I_{\mathrm{FF}}(f_x) \propto |A_{\mathrm{FF}}(f_x)|^2. \tag{7}$$

The I_{FF} expression can be developed to show CBC lobes and inter-lobes power ϵ (omitted to avoid overloading equations):

$$I_{\mathrm{FF}}(f_x) \propto \sum_{k\in\mathbb{Z}} \widetilde{G_T}^2\left(\frac{k}{a}-\alpha\right)\mathrm{sinc}^2\left[3a\left(f_x-\frac{k}{a}\right)\right] + \epsilon \tag{8}$$

All the lobes of the pattern have a $\widetilde{G_{\mathrm{T}}}^2(k/a-\alpha)$ weight, plus a small contribution of the amplitude cross-terms, which in the end depends on the residual tilt α. This situation is illustrated in Fig. 9, where one can see the visible effect of such tilt on the CBC pattern's irradiance, with a comparison from a real data sample extracted from a 1 km measurement.

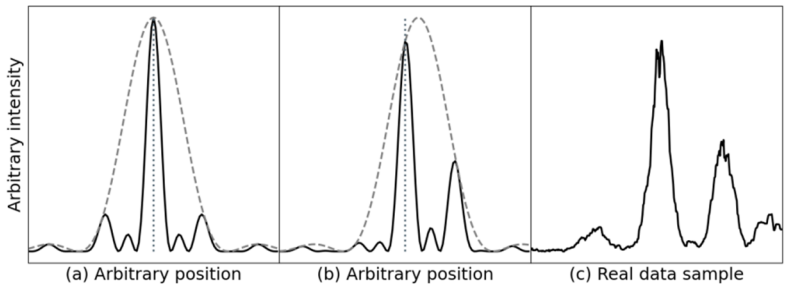

Fig. 9: ((a) and (b)) 1D simulation of the FF Irradiance (black curve). (a) Case of perfect combination with no residual tilt over each channel. (b) A small amount of tilt is added, so that the position of the CBC envelope is slightly shifted, hence the shape of the FF pattern. In both representations, the dashed gray line represents the signal envelope, while the dotted line stands for the supposed target central position. (c) A real irradiance curve has been extracted from experiments for comparison purpose.

This model is consistent with our observations. The residual tip-tilt is responsible for the variation in the irradiance pattern that has been observed as envelope wandering in the locked pattern in both simulation and experimental data.

The case presented here, with a residual common tip-tilt on all pupils, can be easily identified by near field wavefront PISTIL analysis. Indeed, the pistons compensating for a global tip-tilt induced by turbulence can be seen for example in the insert of Fig. 8 (extracted from real data). Let us now compare the corresponding experimental sequences recorded in the NF and FF.

4.3 Experimental analysis of the turbulence-induced phase variation corrected by pistons with NF and FF diagnoses

First, the residual tip-tilt of the atmospheric turbulence in closed loop can be estimated from a FF pattern sequence analysis (with the 60 Hz RAPTOR camera). For each FF image, a "combined beam centroid" or "barycenter displacement" $\left[C_x(t), C_y(t)\right]$ is estimated in the camera reference plane. To minimize bias while estimating the centroid, CBC image sequences have been corrected from camera background noise. Then, the tip-tilt angles are computed using:

$$\alpha_x(t) \approx \frac{C_x(t)}{D}, \quad \alpha_y(t) \approx \frac{C_y(t)}{D}, \tag{9}$$

where D is the distance, $\alpha_x(t)$ the tip, and $\alpha_y(t)$ the tilt, defined according to the x-axis (horizontal) and the y-axis (vertical) relatively to a planar wavefront orthogonal to the propagation direction z. Corresponding tip-tilt values are reported in Fig. 10 (red curves).

Second, as explained in sections 4.1 and 4.2, we estimate a global tip-tilt using the 7 pistons from the PISTIL analysis (Fig. 8). To do so, we fit the 7 pistons with tip-tilt generic functions (or Zernike polynomials, see section 3.2) to derive a rough estimate of the global tip-tilt and therefore the residual tip-tilt per channel. We made sure that the fitting error was kept minimal. If this was not the case, then this would have meant that the explanation in 4.1 was wrong, e.g. the wavefront is not actually distorted by tip-tilts.

The tip-tilt estimates based on centroid (FF) and PISTIL (NF) can now be compared. Fig. 10 shows how these estimates evolve with time at distances of 311 m and 1024 m. The turbulence strengths were $C_n^2 = 2.10^{-14}\ \mathrm{m}^{-2/3}$ and $C_n^2 = 4.10^{-14}\ \mathrm{m}^{-2/3}$, respectively. Red curves show the (residual) tip-tilt estimated by centroid estimation in the FF, whereas blue curves show the same quantity extracted from the PISTIL data. The offsets between those values were removed in order to provide a qualitative comparison.

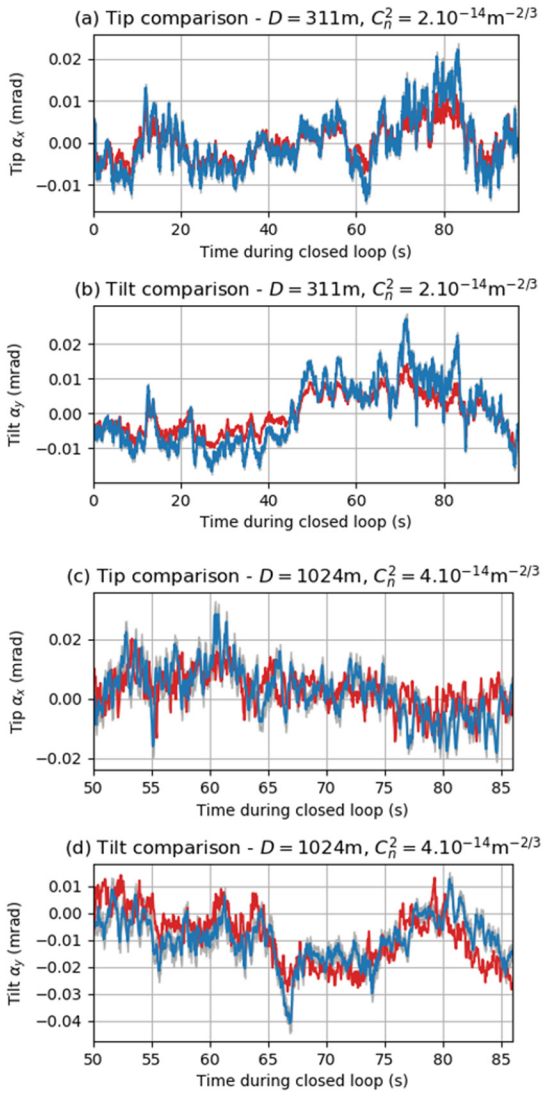

Fig. 10: Comparison of the tip (a,c) and the tilt (b,d) experimental estimates by x, y centroid computing (red curve) in the FF and by PISTIL in the NF (blue curve with fitting error in light gray), during closed-loop time sequences for 311 m (a,b) and 1024 m (c,d). Overall tendencies of both estimates are similar.

The estimation of tip-tilt by these two methods shows a centroid shift on the order of a few mrad around the target center compared to the lobe size, 47 µrad at 311 m and 41 µrad at 1024 m. As we know the magnification of the image by the size of the reflector, we have also deduced the sizes in metric units, 14.6 mm and 41.2 mm for both distances, and the deviation of the centroid is a few millimeters. A variation of more than 20 µrad in total would shift the envelope to the halfway of the inter-lobes distance, as suggested in Fig. 9. Both estimates show very close behavior even though the PISTIL estimate has larger variability and a local offset appears in tilt measurement (Fig. 10b and 10d). This displacement of the beam envelope, monitored either in the FF and now the NF, explains the fluctuations of the power of the central lobe, especially at the 311 m distance where the CBC pattern position was very stable, and where the leakage toward the side lobes was clearly seen (Fig. 6).

Even though similar behaviors have been observed at the 1024 m distance for weak to moderate turbulence level as shown in Fig. 10, most of the data did not show such a clear match because of the turbulence distortion of the CBC pattern when $C_n^2 > 4 \times 10^{-14}$ m$^{-2/3}$. Indeed, as discussed in section 4.1, when r_0 gets smaller than the pupil size, the global tip-tilt and global piston model is no longer valid and higher-order aberrations must be taken into account. This impact of strong turbulences is illustrated by Fig. 6 (h), where the CBC pattern, still noticeable, is the evidence of an active phase locking. Nevertheless, it is also clearly distorted, suffering from global tip-tilt and higher order aberrations. Finally, it results in increasing the centroid estimate uncertainty. In the NF plane, fitting with higher-order aberration functions would have been possible [13], but the comparison with the FF is less straightforward.

To sum up this analysis, for distances 311 m and 1024 m with moderate turbulence ($C_n^2 < 4 \times 10^{-14}$ m$^{-2/3}$), both tip-tilt estimates are in good agreement. These results support the hypothesis that the global tip-tilt, uncompensated by phase pistons in closed-loop, is responsible for the power loss in the central lobe of the FF pattern. These results also validate the NF diagnosis made with the PISTIL interferometer, which suggests that a NF analysis could be sufficient to determine the displacement of the beam envelope without any FF optical equipment. Furthermore, the use of a NF segmented wavefront sensor allows estimating whenever r_0 becomes smaller than the pupil size: estimates do not match anymore, and the wavefront tip-tilt fit error increases quickly.

5. Conclusion

A TIL-CBC laser system made of seven 1.5 µm fiber amplifiers tiled in a hexagonal mesh has been presented. Its LOCSET phase control scheme uses the signal backscattered from the target to extract the relative phase differences between the beams and drive them to zero. The power in the central lobe is thus maximized and therefore the local power deposited on the target. The system showed highly stable CBC patterns at multiple working distances, from laboratory scale (15 m) to outdoor scales of 70 m, 311 m and ultimately 1 km through atmospheric turbulence.

Even though power increase in the central lobe was successfully obtained on the target with TIL-CBC in all configurations, detrimental effects have also been observed. The first observed detrimental effect was power leakage from the central lobe to the side lobes at 311 m and 1024 m distances. In the last case, greater distortions occurred.

For a moderate turbulence condition ($C_n^2 < 4 \times 10^{-14}$ m$^{-2/3}$), we estimated the Fried parameter r_0 that describes the spatial variations of the phase, and deduced that the turbulence was mainly composed of a global tip-tilt in our experiments. Assuming that this global tip/tilt is partially compensated by individual pistons, a simple CBC model has been proposed to explain the observed power leakage. According to this model, the FF pattern is made of a spot array modulated by an envelope. The spot array is efficiently stabilized by the piston feedback loop in all conditions, whereas the envelope wanders because of residual turbulence effects. This wandering is responsible for power-leakage from the central lobe to the side lobes and cannot be compensated for, as no tip/tilt correction is included in LASBE testbed.

A NF PISTIL interferometer was embedded in the emitter to measure piston compensations of the atmospheric turbulence by LOCSET feedback. It provided an estimate of the global turbulence-induced tip-tilt over the LASBE pupil, by fitting tip and tilt functions over the wavefront made of the beams' pistons. This global tip-tilt estimate has been validated against the FF estimate of beam envelope displacement. This confirms the aforementioned model, especially at the 311 m distance where no distortions other than envelope wandering were reported.

Future works involve comparison of turbulence strength and PISTIL-measured piston temporal power spectrum [41] as well as comparison of tip-tilt fit accuracy and precise estimation of r_0. Alongside these on-board turbulence characterizations, the PISTIL interferometer could become a complementary element of the phase-controller, in addition to the LOCSET, to reduce power-leakage in the FF without any on-target device using a global

tip-tilt actuator. Finally, distant perspective to this work could be to consider co-phasing with the LOCSET algorithm on a non-cooperative target.

Acknowledgement

The authors want to thanks B. Augère, D. Goular, C. Planchat, D. Fleury, J.-M. Conan, C. Bellanger and J. Primot from ONERA.

Disclosures

The authors declare that there are no conflicts of interest related to this article.

Data availability

Data underlying the results presented in this paper are not publicly available at this time but may be obtained from the authors upon reasonable request.

References

1. W. P. Leemans, "White paper of the ICFA-ICUIL joint task force: High power laser technology for accelerators," ICFA Beam Dyn. Newslett. **56**, 10–88 (2011).
2. V. C. Coffey, "High-Energy Lasers: New Advances in Defense Applications", Optics & Photonics News (**25**), 2014.
3. P. Sprangle, B. Hafizi, A. Ting, and R. Fischer, "High-power lasers for directed-energy applications," Appl. Opt. **54**, F201-F209 (2015).
4. A. R. Chraplyvy, "Limitations on lightwave communications imposed by optical-fiber nonlinearities," in Journal of Lightwave Technology **8**(10), 1548-1557, (1990).
5. Y. Jaouën, G. Canat, S. Grot, S. Bordais, "Power limitation induced by nonlinear effects in pulsed high-power fiber amplifiers," C. R. Physique J, **7**(2), (2006).
6. A. Kobyakov, M. Sauer, and D. Chowdhury, "Stimulated Brillouin scattering in optical fibers," Adv. Opt. Photon. **2**, 1-59 (2010).
7. T. Y. Fan, "Laser beam combining for high-power, high-radiance sources," IEEE JSTQE, **11**(3), 567-577, (2005).
8. A. Flores, T. M. Shay, C. A. Lu, C. Robin, B. Pulford, A. D. Sanchez, D. W. Hult and K. B. Rowland, "Coherent beam combining of fiber amplifiers in a kW regime," *CLEO: 2011-Laser Science to Photonic Applications* (pp. 1-2) (2011).
9. L. Lombard, J. Le Gouët, P. Bourdon, G. Canat. "Coherent Beam Combining of Pulsed Fiber Amplifiers in the Long-Pulse Regime (Nano- to Microseconds)," In Coherent Laser Beam Combining, Chapter **8**, Wiley-VCH Verlag GmbH & Co. KGaA, (2013).
10. M. A. Vorontsov and S. L. Lachinova, "Laser beam projection with adaptive array of fiber collimators. I. Basic considerations for analysis," J. Opt. Soc. Am. A **25**, 1949-1959 (2008).
11. S. L. Lachinova and M. A. Vorontsov, "Laser beam projection with adaptive array of fiber collimators. II. Analysis of atmospheric compensation efficiency," J. Opt. Soc. Am. A **25**, 1960-1973 (2008).
12. R. Tao, Y. Ma, L. Si, X. Dong, P. Zhou, and Z. Liu. "Target-in-the-loop high-power adaptive phase-locked fiber laser array using single-frequency dithering technique," App. Phys. B **105**(2), (2011).
13. S. L. Lachinova, M. A. Vorontsov, "Wavefront sensing and adaptive control in phased array of fiber collimators," Proc. SPIE 7924, Atmospheric and Oceanic Propagation of Electromagnetic Waves V, 79240F (2011).
14. Z.M. Huang, C.L. Liu, J.F. Li, D.Y. Zhang, H.F. Wang, Y.Q. Luo, Q.Q. Hu, "Numerical analysis of coherent combination for fiber lasers and application to beam steering," Laser Phys. **22,** 1347–1352 (2012).
15. J. E. McCrae Jr., N. Van Zandt, S. J. Cusumano, S. T. Fiorino, "Simulation of atmospheric turbulence compensation through piston-only phase control of a laser phased array," Proc. SPIE 8733, Laser Technology for Defense and Security IX, 873311 (2013).
16. M. Hyde, J. Wyman, and G. Tyler, "Rigorous investigation of the array-tilt aberration for hexagonal, optical phased arrays," Appl. Opt. 53, 2416-2424 (2014).
17. M. F. Spencer, D. E. Thornton, M. W. Hyde and J. Bos, "Piston phase compensation of tiled apertures in the presence of turbulence and thermal blooming," *IEEE Aerospace Conference*, 1-20 (2014).
18. J. Wyman and M. W. Hyde, "Detection and correction of stair mode across an optical phased array," *IEEE Aerospace Conference*, 1-10 (2014).
19. J. E. McCrae and S. T. Fiorino, "Simulation of array tilt effects in laser phased arrays," *IEEE Aerospace Conference*, 1-7 (2016).
20. J. K. Jabczyński, P. Gontar, "Impact of atmospheric turbulence on coherent beam combining for laser weapon systems," Defence Technology, (2020).

21. X.L. Wang, Y.X. Ma, P. Zhou, H.T. Ma, X. Li, X. X. Xu and Z. J. Liu, “Coherent beam combining of two W-level fiber amplifiers in turbulence atmospheric environment based on stochastic parallel gradient descent algorithm,” Laser Phys. **19,** 984–988 (2009).
22. Yanxing Ma, Pu Zhou, Rumao Tao, Lei Si, and Zejin Liu, "Target-in-the-loop coherent beam combination of 100 W level fiber laser array based on an extended target with a scattering surface," Opt. Lett. **38**, 1019-1021 (2013).
23. T. M. Shay, V. Benham, J. T. Baker, A. D. Sanchez, D. Pilkington and C. A. Lu, “Self-Synchronous and Self-Referenced Coherent Beam Combination for Large Optical Arrays,” in IEEE JSTQE, vol. 13, no. 3, pp. 480-486, (2007).
24. B. Bennaï, L. Lombard, V. Jolivet, C. Delezoide, E. Pourtal, P. Bourdon, G. Canat, O. Vasseur and Y. Jaouën, “Brightness scaling based on 1.55 μm fiber amplifiers coherent combining,” Fiber and integrated optics, **27**(5), 355-369, (2008).
25. T. Weyrauch, M. A. Vorontsov, G. W. Carhart, L. A. Beresnev, A. P. Rostov, E. E. Polnau, and J. J Liu, "Experimental demonstration of coherent beam combining over a 7 km propagation path," Opt. Lett. **36**, 4455-4457 (2011).
26. T. Weyrauch, M. A. Vorontsov, J. Mangano, V. Ovchinnikov, D.Bricker, E.E. Polnau, and A. P. Rostov, "Deep turbulence effects mitigation with coherent combining of 21 laser beams over 7 km," Opt. Lett. **41**, 840-843 (2016).
27. M. A. Vorontsov, T. Weyrauch, S. Lachinova, T. Ryan, A. Deck, M. Gatz, V. Paramonov, and G. W. Charhart, “Coherent Beam Combining and Atmospheric Compensation with Adaptive Fiber Array Systems,” In Coherent Laser Beam Combining, Chapter 6,Wiley-VCH Verlag GmbH & Co. KGaA, (2013).
28. B. Pulford, T. Shay, and J. Baker, “Phase locking an array of fiber amplifiers onto a remote object”, *CLEO/QELS: 2010-Laser Science to Photonic Applications*, 4–5, (2010).
29. M. Vorontsov, T. Weyrauch, S. Lachinova, M. Gatz, and G. Carhart, “Speckle-metric-optimization-based adaptive optics for laser beam projection and coherent beam combining,” Opt. Lett. **37**, 2802-2804 (2012).
30. C. Geng, W. Luo, Y. Tan, H. Liu, J. Mu, and X. Li, “Experimental demonstration of using divergence cost-function in SPGD algorithm for coherent beam combining with tip/tilt control,” Opt. Express **21**, 25045-25055 (2013).
31. F. Li, C. Geng, G. Huang, Y. Yang, X. Li and Q. Qiu. “Experimental Demonstration of Coherent Combining With Tip/Tilt Control Based on Adaptive Space-to-Fiber Laser Beam Coupling,” IEEE Photonics Journal **9**, 1-12 (2017).
32. M. Deprez, C. Bellanger, L. Lombard, B. Wattellier, and J. Primot, “Piston and tilt interferometry for segmented wavefront sensing,” Opt. Lett. **41**, 1078-1081 (2016).
33. M. Deprez, B. Wattellier, C. Bellanger, L. Lombard, and J. Primot, “Phase measurement of a segmented wave front using PISton and TILt interferometry (PISTIL),” Opt. Express **26**, 5212-5224 (2018).
34. B. Rouzé, J. Primot, P. Lanzoni, F. Zamkotsian, F. Tache, and C. Bellanger, “High-dynamic segmented mirror metrology by Two-Wavelength PISTIL interferometry: demonstration and performance,” Opt. Express **28**(22), 32415-32425 (2020).
35. B. Rouzé, J. Primot, F. Zamkotsian, P. Lanzoni, C. Bellanger, “PISTIL interferometry: a modular, plug-and-play metrology mean for diagnosis of coherently combined laser arrays,” Proc. SPIE 11665, Fiber Lasers XVIII: Technology and Systems, 116651K (2021).
36. J. Davis, and W. J. Tango. “Measurement of the Atmospheric Coherence Time.” Publications of the Astronomical Society of the Pacific **108**(723), (1996).
37. L. Lombard, G. Canat, A. Durecu, and P. Bourdon, “Coherent beam combining performance in harsh environment,” Proc. SPIE 8961, Fiber Lasers XI: Technology, Systems, and Applications, 896107 (2014).
38. Robert J. Noll, “Zernike polynomials and atmospheric turbulence*,” J. Opt. Soc. Am. **66**, 207-211 (1976).
39. D. L. Fried, “Statistics of a Geometric Representation of Wavefront Distortion,” J. Opt. Soc. Am. A, **55**(11), 1427– (1965).
40. R. K. Tyson, “Sources of Aberrations” in Principles of Adaptive Optics, Ed. Robert K. Tyson Academic Press (1991).
41. J.-M. Conan, G. Rousset, and P.-Y. Madec, “Wave-front temporal spectra in high-resolution imaging through turbulence,” J. Opt. Soc. Am. A **12**, 1559-1570 (1995).